

# Large-Scale Silicon Photonic MEMS Switch

*Sangyoon Han*

Electrical Engineering and Computer Sciences  
University of California at Berkeley

Technical Report No. UCB/EECS-2015-42

<http://www.eecs.berkeley.edu/Pubs/TechRpts/2015/EECS-2015-42.html>

May 1, 2015



Copyright © 2015, by the author(s).  
All rights reserved.

Permission to make digital or hard copies of all or part of this work for personal or classroom use is granted without fee provided that copies are not made or distributed for profit or commercial advantage and that copies bear this notice and the full citation on the first page. To copy otherwise, to republish, to post on servers or to redistribute to lists, requires prior specific permission.

#### Acknowledgement

This work was supported in part by the National Science Foundation Center for Integrated Access Network (CIAN) under grant #EEC-0812072, National Science Foundation Center for Energy Efficient Electronics Science (E3S) under NSF Award 0939514, and Defense Advanced Research Project Agency (DARPA)'s Electronic-Photonic Heterogeneous Integration (E-PHI) program.

---

# **Large-Scale Silicon Photonic MEMS Switch**

by Sangyoon Han

---

## **Research Project**

Submitted to the Department of Electrical Engineering and Computer Sciences,  
University of California at Berkeley, in partial satisfaction of the requirements for the  
degree of **Master of Science, Plan II**.

Approval for the Report and Comprehensive Examination:

### **Committee:**

---

Professor Ming C. Wu  
Research Advisor

---

(Date)

\* \* \* \* \*

---

Professor Liwei Lin  
Second Reader

---

(Date)

## **ABSTRACT**

Fast optical circuit switches with large port count will allow flexible bandwidth allocation in datacenter networks by augmenting electrical packet switching. Reported herein is the development of a microsecond-speed optical circuit switch with  $50 \times 50$  port counts implemented on silicon photonics platform using MEMS-actuated directional couplers. The switch contains a number of innovative enhancements: fast switching speed ( $2.5 \mu\text{s}$  response time) and high on-off extinction ratio (25 dB), which are complimented by a small footprint ( $9 \times 9 \text{ mm}^2$ ) and simple fabrication process (only three lithography steps). This prototype switch port-count appears capable of being scaled up to  $100 \times 100$  and beyond.

## 1. INTRODUCTION

Due to the increase of data traffic in datacenters, bandwidth management of networks has become a serious issue and enhancing the performance of datacenters a key goal. One promising way to manage bandwidth in datacenters is to use optical circuit switches to allocate bandwidth between servers [1,2]. By connecting the servers in datacenters using optical networks and reconfiguring the connections between the servers by optical circuit switches, one can efficiently manage dynamically varying traffic between servers. Three-dimensional micro-electro-mechanical systems (MEMS) switches have been used in the past for this application, but the advantage of using them was limited because of their slow switching time (on the order of 1-10ms). The switching time of silicon photonic switches are on the order of microsecond or less and were initially deemed as a good candidate for this type of application. In addition, a silicon photonics platform provides dense integration of components and a seamless interface to CMOS drivers [3]. However, such applications were limited up to an  $8\times 8$  port count due to its architecture (cascaded  $2\times 2$ ), thus incurring a high optical insertion loss.

This paper reports on a highly-scalable optical switch architecture built on a silicon photonic platform using MEMS technology. The scalability of the switch on a  $50\times 50$  switch network is demonstrated. The small mass of silicon photonic components allow fast actuation of the MEMS, which result in a fast response of the switch. In addition, by changing the light path geometrically as opposed to using refractive index tuning, the MEMS actuation results in a high extinction ratio of the switch and low leakage optical loss.

## 2. SWITCH DESIGN

### A. Switch Architecture

Figure 1a illustrates the architecture of the prototype switch reported herein. Silicon waveguides were used to form an optical crossbar network. Light is coupled from fibers to grating couplers, which are located at the end of the switch network. A MEMS actuator with movable directional couplers is located at each mesh of the crossbar network and forms one unit cell; the actuators can be actuated independently to control the light path.

Each unit cell is capable of two states: the Through-state and the Drop-state. When the cell is in Through-state, the MEMS actuator is bent out-of-plane, and the light comes into the in port of the cell and simply follows the waveguide to the Through port. When the cell is in Drop-state, however, the MEMS actuator with waveguide attached is initiated to form two pairs of directional couplers, which allows the light to couple between the waveguides and proceeds to the Drop port. By selecting the state of the each unit cell, it is possible to route simultaneously light from any input grating couplers to any output grating couplers. For an  $N\times N$  switch, this architecture has  $N^2$  of switch unit cells, which can be controlled individually. The advantage of this architecture is that for any given light path, the light goes through switching action only once, regardless of the port count of the switch network;

the rest of the time it stays in passive waveguides. Since the switching action produces more power leakage and insertion loss than guiding through passive waveguides, this prototype switch architecture has advantage of low insertion loss when considering scaling the size of the switch.

The optical switch architecture reported herein had path-dependent insertion loss variation, which is inherent in optical crossbar networks. The optical insertion loss is from the result of passive waveguides and the waveguide crossings that provide the connection between the unit cells. Ideally, the insertion loss from the waveguides should be negligible compared to the insertion loss from the waveguide crossings. Most of the waveguide loss is due to sidewall roughness-induced scattering, which is fabrication process dependent. Practically, the insertion loss from waveguides can be reduced by improving the etch profile of the fabrication process [4] and additional post-processing methods [5] to reduce sidewall roughness of the waveguide.

That said, waveguide-crossing loss is mostly a result of optical scattering due to the guiding profile change at the crossing point. For the longest optical path for an  $N \times N$  crossbar switch, there are  $2N$  of waveguide crossings that the light needs to pass through; therefore, the longest path insertion loss of the switch linearly scales with the loss of a waveguide crossing. Thus, very careful design of waveguide crossing is required to reduce the insertion loss of the prototype switch architecture.

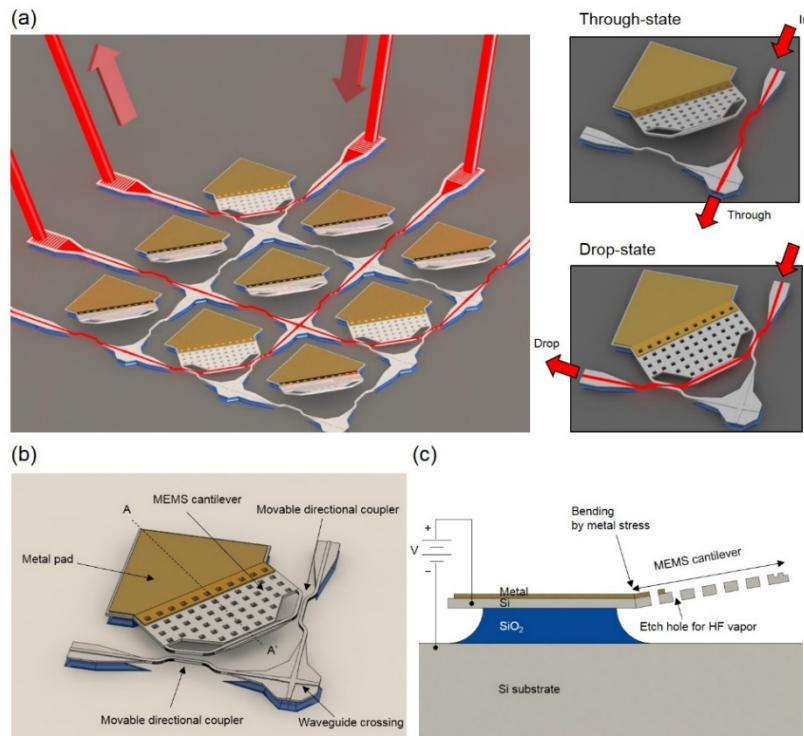


**Figure 1** (a) Schematic of the switch architecture; (b) schematic of the switch unit cell; and (c) cross-section view of the switch unit cell.

## B. Switch Unit-Cell

Figure 1b shows schematically the unit cell structure of the prototype switch. It consists of one MEMS cantilever actuator with metal probing pad, two pairs of movable directional couplers, one waveguide crossing, ridge waveguides, and waveguide tapers. One pair of directional couplers consists of two waveguides with same width and length. One waveguide of the pair is connected to a ridge waveguide and a waveguide crossing, and are anchored on silicon dioxide layer. The other waveguide of the pair is connected to the MEMS cantilever actuator and moves with the actuator. The MEMS cantilever actuator can be moved vertically by applying the voltage between the silicon substrate and the actuator through the metal pad. By changing the vertical location of the movable waveguide using the MEMS actuator, it is possible to control the coupling between the two waveguides. When the actuator comes down and the movable waveguide is in the same plane as the fixed waveguide, strong coupling occurs between the two waveguides, forming a pair of directional couplers. In this configuration, light coming from one of the waveguide couples with the other waveguide. By choosing the appropriate length and the width of the waveguides, light from one waveguide transfers completely to the other.

## C. Low Loss Waveguide Crossing

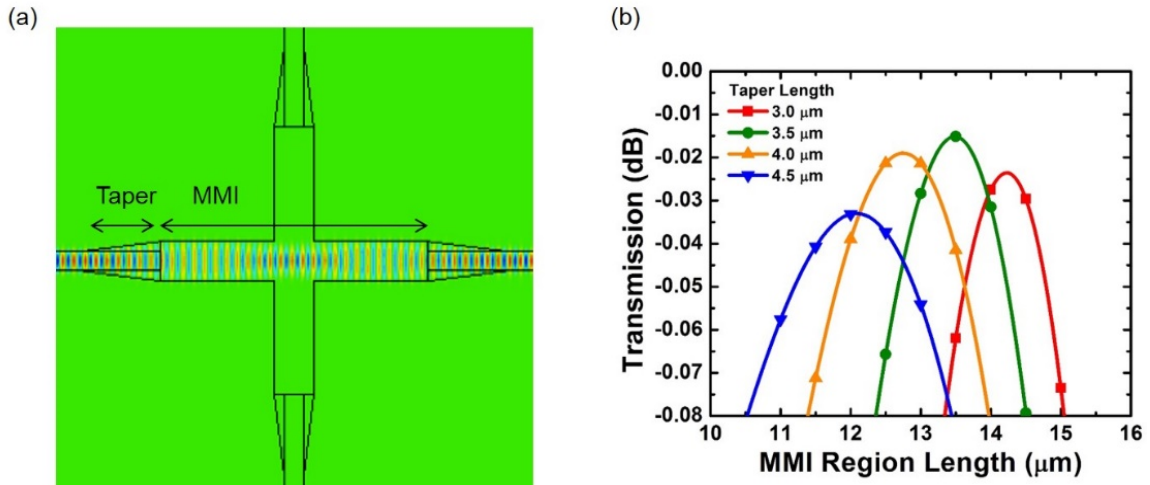


**Figure 2** (a) Optical mode profile of the time domain simulation of the waveguide crossing with the optimal dimension; and (b) transmission loss of the waveguide crossing with various dimensions.

The major loss mechanism of the waveguide crossing is the optical scattering at the crossing point. The lateral guiding of the optical mode abruptly changes at the point where the two orthogonal waveguides meet. To address this issue, the interaction between optical mode and the guiding at the crossing point is reduced by focusing the optical mode at the crossing point by utilizing a Multi-Mode Interference (MMI) pattern; see Figure 2a. Interference of the first mode and third mode (second odd mode) of the waveguide can

create a focusing pattern at the center of the waveguide. In order to excite the two modes, the waveguide width was gradually tapered from 500 nm to 2  $\mu\text{m}$ . Conducting a parameter sweep of the taper length and the MMI length (Figure 2b) facilitated finding the optimal point that has the lowest insertion loss. The mode profile of a time domain simulation is shown in Figure 2a, and the parameter sweep result is shown in Figure 2b. The optimal design was found to have a 3.5- $\mu\text{m}$  taper length and a 13.5- $\mu\text{m}$  MMI length; the insertion loss at this dimension was 0.015 dB.

#### D. Movable Directional Coupler

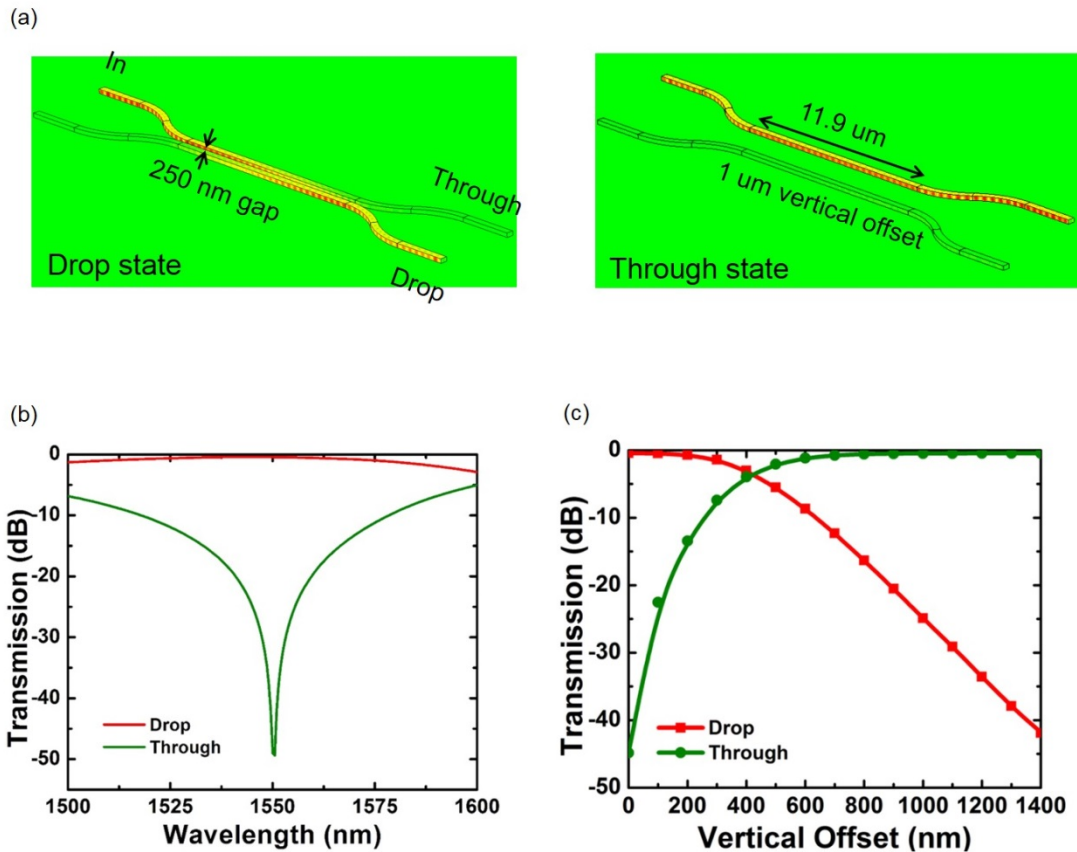


Figure 3. (a) Optical mode profile of directional coupler at Drop-state (left) and Through-state (right); (b) spectral response of a Movable directional coupler; and (c) transmission characteristics of a Movable directional coupler with different vertical offsets.

Figure 3a shows the mode profile of a time domain simulation of a movable directional coupler. A movable directional coupler consists of two identical waveguides in parallel. The width and the thickness of the waveguides are 350 nm and 220 nm, respectively. The length of the waveguides is 11.9  $\mu\text{m}$ . The movable directional coupler has two states: the Through-state and the Drop-state. At Drop-state, the two waveguides are placed at the same

plane with a 250-nm gap. In this configuration, the two waveguides are coupled, and light from one waveguide completely transfers to the other waveguide. In the Through-state, however, two waveguides are vertically away from each other by 1  $\mu\text{m}$ . In this configuration, the two waveguides no longer coupled, and the light simply follows the waveguide, the path the light had originally traveled. Figure 3b shows the spectral response of the movable directional coupler in a Drop-state. The extinction ratio between the Drop port and the Through port is 50 dB at a 1550-nm wavelength.

Figure 3c shows the simulated transmission characteristics of the movable directional coupler with different vertical offsets. At 0- $\mu\text{m}$  vertical offset, when the two waveguides are in the same plane, optical power transfers to the Drop port with negligible loss and only -45 dB (relative to the input power) of optical power goes to the Through port. At 1- $\mu\text{m}$  vertical offset, however, most of the optical power goes to the Through port and only -25 dB (relative to the input power) of optical power goes to the Drop port.

### E. MEMS Actuator Design

Figure 1c shows a cross section of the MEMS actuator, which controls the vertical offset of the movable directional coupler. The actuator moves up and down due to the electrostatic force between the substrate and the cantilever. The voltage applied between the cantilever and the silicon substrate controls the amount of the electrostatic force. The fixed side of the cantilever is extended and anchored on a  $\text{SiO}_2$  layer. There is a metal coating on top of the extended part of the cantilever, and the stress in the metal coating [6] bends the cantilever upward by 1  $\mu\text{m}$  in the absence of any voltage bias. . There are etch holes on the cantilever for the HF vapor gas to flow, which etches  $\text{SiO}_2$  layer to release the cantilever in the air. A capacitive cantilever beam model was used to design the MEMS actuator. The thickness of the beam was set at 220 nm, which is the thickness of silicon layer of Silicon-On-Insulator (SOI) wafer used for fabricating the prototype switch. The gap between the cantilever and the substrate was set as 3  $\mu\text{m}$ , which is the thickness of the buried oxide layer of the SOI wafer. The length of the cantilever was chosen to be 40  $\mu\text{m}$  to obtain both fast actuation speed and low-voltage operation. The resonant frequency [7] and the pull-in voltage [8] of the cantilever were calculated using the following equations and values:

$$f_{res} = \frac{3.52}{2\pi} \sqrt{\frac{Et^2}{12\rho l^4}} \quad (1)$$

$$V_{pull-in} = \sqrt{\frac{3Et^3 z_0^3}{10\epsilon_0 l^4}}, \quad (2)$$

where  $E = 150$  GPa (Young's modulus of Si),  $t = 220$  nm (thickness of the cantilever),  $\rho = 2.32$   $\text{g}\cdot\text{cm}^{-3}$  (density of silicon),  $l = 40$   $\mu\text{m}$  (length of the cantilever), and  $z_0 = 3$   $\mu\text{m}$  (gap between the cantilever and the substrate). The resonant frequency and the pull-in voltage were calculated as 179 kHz and 24 V, respectively.

### 3. EXPERIMENTS

#### A. Fabrication

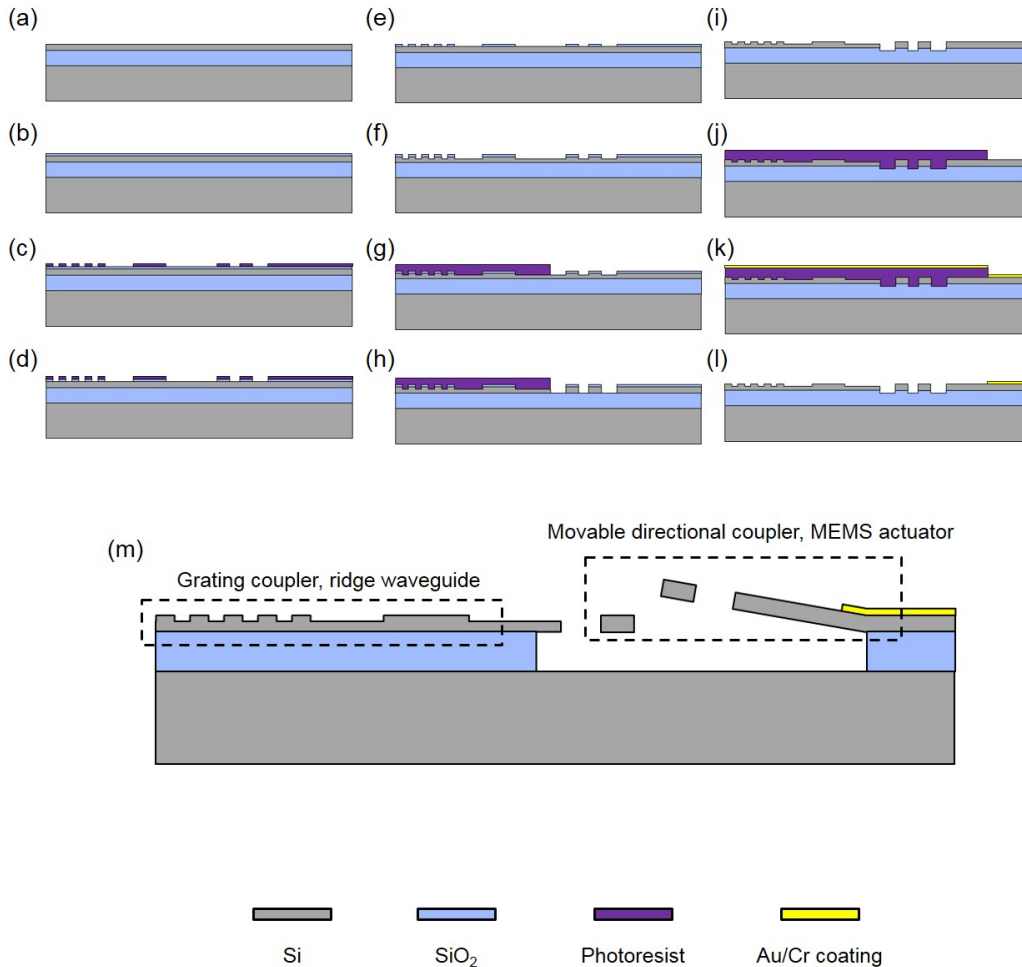


**Figure 4** (a) A fresh SOI wafer with 220-nm silicon device layer and a 3- $\mu\text{m}$  buried oxide layer; (b) 100 nm low-temperature oxide (LTO) deposited on top of the wafer as the etching hardmask layer; (c) the photoresist patterned by the first lithography step; (d) LTO layer etched; (e) photoresist removed; (f) the device layer etched 70 nm deep; (g) photoresist patterned by the second lithography step; (h) the device layer etched all the way down to the buried oxide layer; (i) photoresist removed; (j) photoresist patterned by the third lithography step; (k) metal (Cr/Au) evaporated on the wafer; (l) metal lifted off; and (m) chip released by HF vapor etching.

The switch chip was fabricated at the University of California, Berkeley, Marvell Nanofabrication Laboratory, using the standard silicon photonic process and HF vapor release process. Figure 4 shows the flow of the fabrication process. First, to construct a

hardmask for the first etch step, a 100-nm-thick SiO<sub>2</sub> layer was deposited on a SOI wafer with a 220-nm thick device layer and 3- $\mu$ m buried oxide layer. Then photoresist coating was applied on top of the hardmask and patterned with a deep UV stepper. The hardmask was etched all the way down to the device layer using an ICP (Inductively Coupled Plasma) etcher. The photoresist was removed after patterning the hardmask, and the device layer was etched 70 nm deep with a TCP (Transformer Coupled Plasma) etcher. While retaining the remaining hardmask, a second lithography was done similar to the first lithography, and then the device layer was etched all the way down to the buried oxide layer using a TCP etcher. The last lithography step—for the metal lift-off process—was followed after removing the photoresist used for the second lithography step. An application of 5-nm-thick chrome and 30-nm-thick gold was evaporated on the wafer; acetone was used to lift-off the metal. Finally, HF (hydrofluoric acid) vapor etching was used to undercut the buried oxide under the waveguides and actuators to release them into the air.

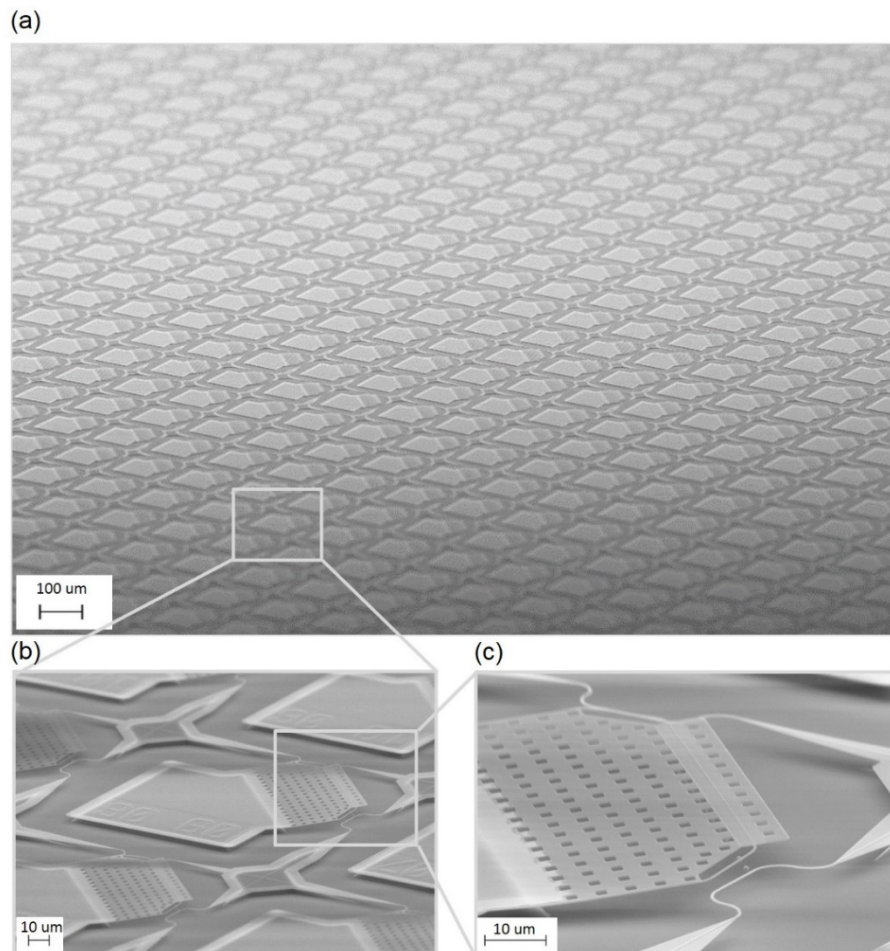


**Figure 5** (a) SEM image of 50×50 switch chip array; (b) zoomed-in SEM image of the array; and (c) SEM of a switch unit cell.

Figure 5 shows the SEM images of the fabricated switch chip. The unit cell size of the switch is  $160 \times 160 \mu\text{m}^2$ ; 2500 switch cells with MEMS actuated directional couplers were monolithically integrated on a  $9 \times 9 \text{mm}^2$  chip area.

## B. Measurement Method

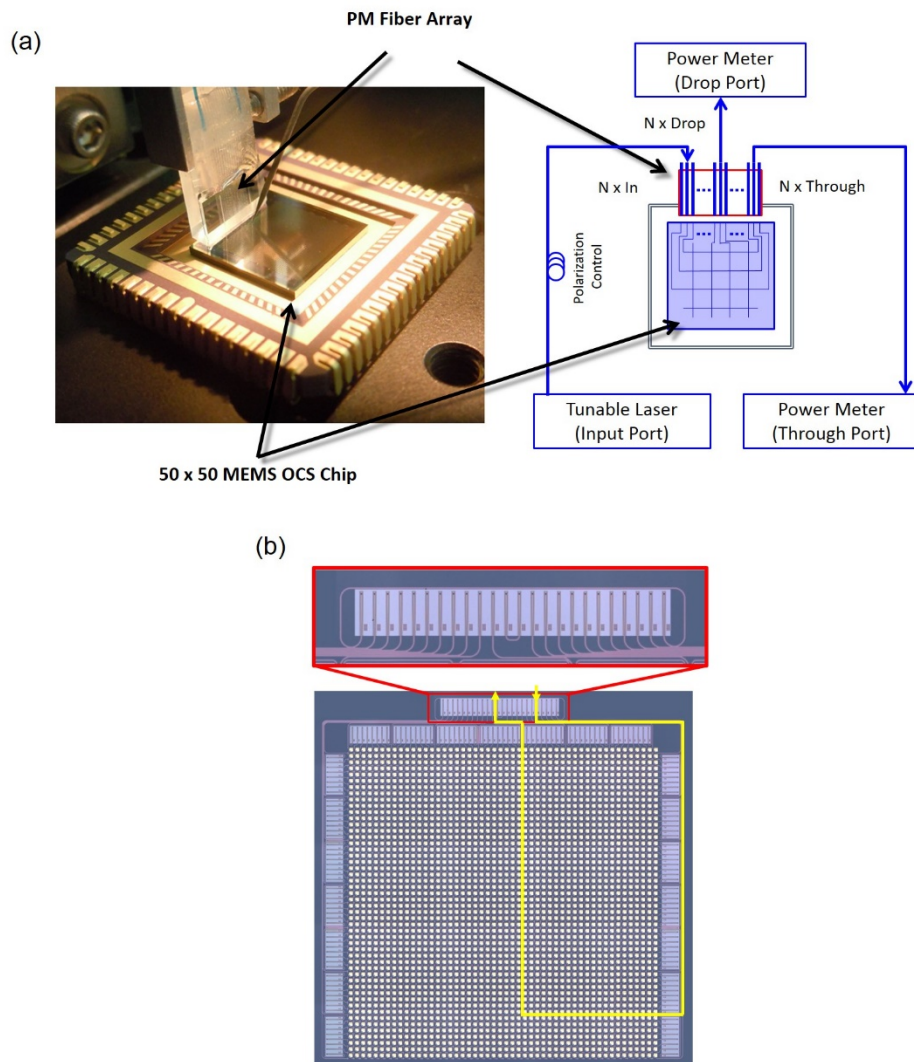


**Figure 6** (a) Photograph (left) and schematic (right) of the switch chip mounted on a chip carrier with a fiber array aligned to it; and (b) optical microscope image of the switch chip with an example of a light path (yellow line).

Figure 6a shows a photograph and a schematic of the switch chip on the measurement set-up. The switch chip was mounted on a chip carrier, and a set of fiber array was used to couple light into the chip. A tungsten probe with a  $5\text{-}\mu\text{m}$ -radius tip was used to electrically

probe the switch cells. The fiber array was attached to the alignment stage with six degrees-of-freedom to allow precise alignment between the fiber array and the switch chip. In order to measure the large switch array using a single fiber array, a grating coupler array was located at one side of the chip that routed waveguides to the subset of the switch array (Figure 6b). The fibers in the fiber array were terminated with FC/APC connectors. The connectors were connected to a tunable laser source and optical power meters to characterize the properties of the switch.

### C. Transmission Characteristics of the Switch with Voltage Bias

The transmission characteristics of the switch cells were measured when different voltage bias applied. Figure 7 shows measured transfer curve with voltage bias from 0 V to 14.2 V. At 14 V, the switch reached the point where the extinction ratio between the Drop port and the Through port was at its maximum. The on-off extinction ratio for both the Drop port and the Through port was larger than 25 dB. The graph also shows that the transmitted power to the Drop port and the Through port rapidly changes between 10 V to 14 V, which allows the switch to operate with low actuation voltage with DC bias added.

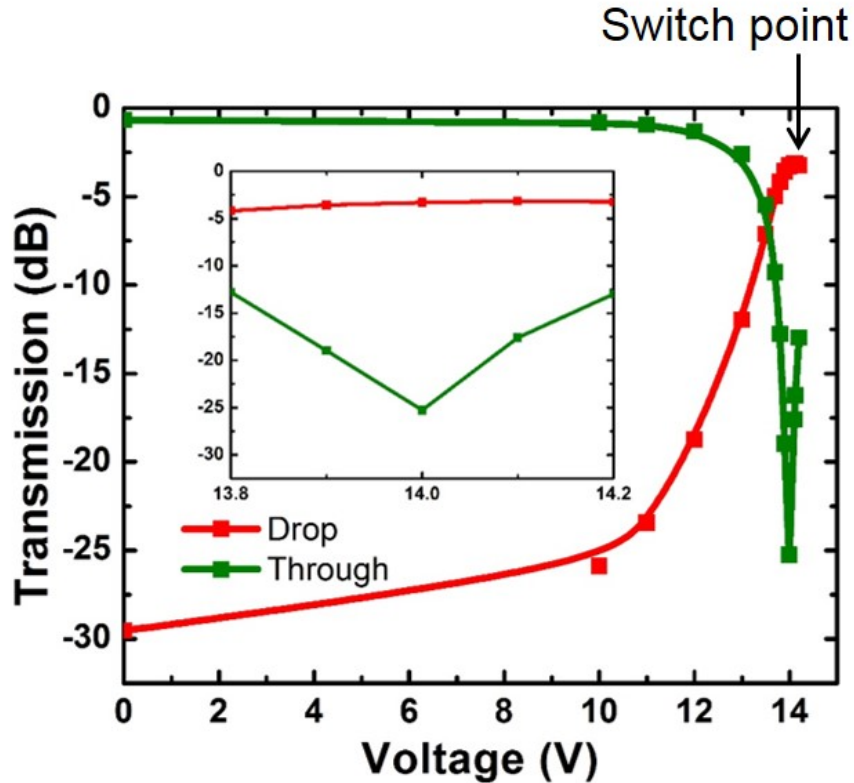


Figure 7 Measured transfer characteristic of the switch with different voltage bias.

#### D. Spectral Response of the Switch

Figure 8 shows both the simulated and measured spectral response of the switch unit cell at the optimal switching point. Since there are two MEMS-actuated directional couplers for the Drop port path, the spectral response of the Drop port of the unit cell is multiplication of two MEMS-actuated directional couplers. Thus for the simulated value, two cascaded identical directional couplers were assumed for the Drop port. The wavelength range measured was limited by a tunable laser, which had a tuning range from 1460 nm to 1580 nm. As shown in the graph, the measured spectral response of the switch unit cell was in good agreement with the simulated values. The largest extinction ratio between the Drop port and the Through port was near 1550 nm for both simulated and measured result. The small discrepancy between the measurement result and the simulation result was largely because of the non-ideal width of the waveguides in the directional couplers.

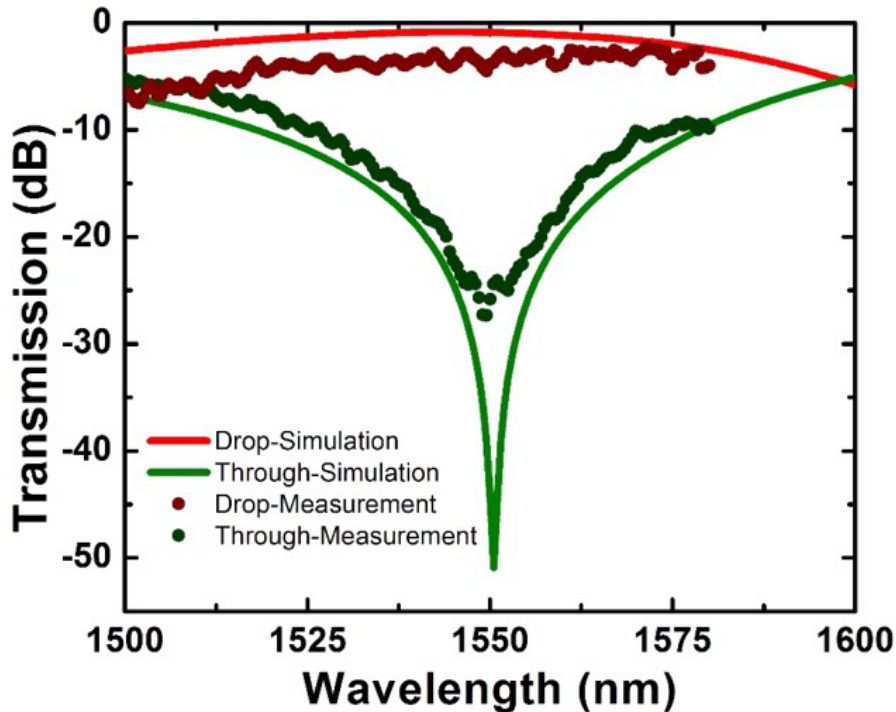


Figure 8 Measured (dots) and simulated (lines) spectral response of the switch unit cell.

#### E. Switch Temporal Response

Figure 9a shows the temporal response of the switch with respect to the step voltage applied to the switch. The switch reached the 90% of the set power within 2.5  $\mu\text{s}$  for turning on, and reached 10% of the set power within 3.8  $\mu\text{s}$  for turning off. There were some ripples

in the optical power trace due to the vertical ringing of the MEMS actuator. The ringing can be suppressed by using a more sophisticated driving voltage shape.

Figure 9b shows the frequency response of the MEMS actuator. The vertical motion of the MEMS actuator was measured in response to the bias voltage with different frequencies by using a Laser Doppler Vibrometer (LDV). The resonance peak of the vibration was near 163 kHz, which is in good agreement with the calculated resonant frequency (179 kHz). For future consideration, a switch with a faster response time is achievable with stiffer MEMS actuators with higher resonant frequencies.

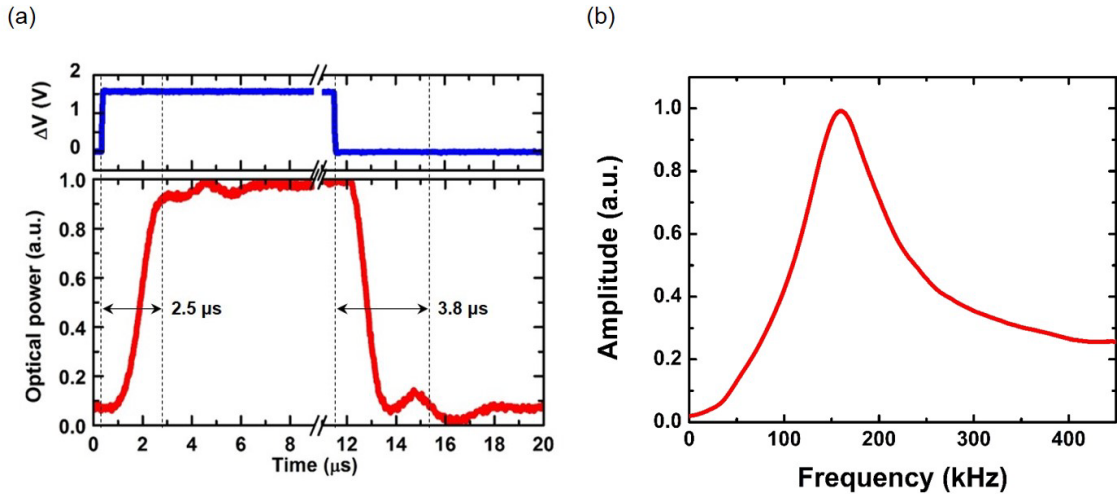


Figure 9 (a) Measured time response of the switch to the step voltages applied; and (b) measured frequency response of the MEMS actuator.

## F. Optical Insertion Loss of Switch

In order to characterize the path-dependent loss of the prototype switch, the insertion loss of several optical paths was measured with different path lengths (Figure 10a). The grating coupler loss was measured on grating coupler test structures and then subtracted from the measured values. Due to the fabrication variation on the switch chip, the average waveguide width in the movable directional couplers was defined to be 430 nm. The insertion loss of the longest path, which contains 98 cells in the Through-state and one cell in the Drop-state, was 27.5 dB. By linear fitting of the measured insertion loss data, it was possible to extract the insertion loss of a Through-state cell, which corresponds to the slope of the fitted line: the insertion loss of a Through-state cell was 0.253 dB/cell. The  $Y$ -intercept of the fitted line was -2.47 dB, corresponding to Drop-state loss of the switch cell. Insertion loss of a Drop-state cell can be eliminated with better dimension control of movable directional couplers at the lithography step.

In the prototype switch architecture, there is only one Drop-state cell for any given path; therefore, Drop-state loss does not scale as the switch size increases. However, there are  $2N-2$  of Through-state cells for the longest optical path in the  $N \times N$  switch. Thus, the Through-state cell loss is a major issue to address in scaling the switch size. The Through-

state loss is due to two factors: loss of waveguide crossings and propagation loss of the waveguides. In order to characterize the loss of the waveguide crossings, waveguide-crossing loss test structures were fabricated, which consist of back-to-back waveguide crossings in series. There were different numbers of waveguide crossings in different test structures. The loss of the each test structure was measured, and the loss per one waveguide crossing was extracted by linear fitting of the measured loss (Figure 10b). The loss per waveguide crossing was extracted as 0.038 dB. The propagation loss of the waveguide was mainly from the result of the optical scattering loss due to roughness on the sidewall of the waveguides; hence, this loss can be reduced by fabricating the switch with a more advanced fabrication process which produces a smooth etch profile for the waveguide sidewall.

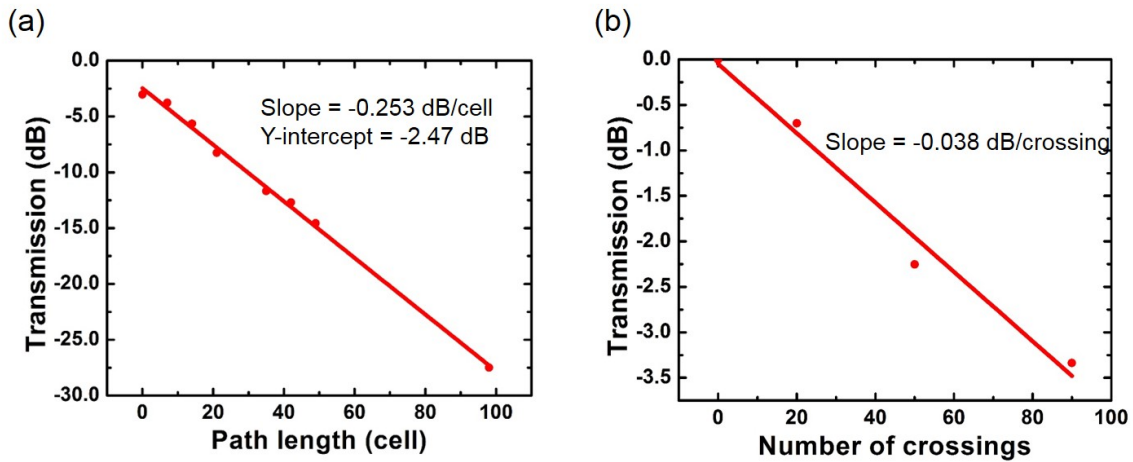


Figure 10 (a) Measured insertion loss of several optical paths with different path lengths; and (b) measured insertion loss of the waveguide-crossing test structures with different numbers in series.

## 4. CONCLUSIONS

The design, fabrication, and characterization of a  $50 \times 50$  silicon photonics MEMS switch is reported, where 2500 ( $50 \times 50$ ) switching cells with MEMS actuators were integrated on a  $9 \times 9$  mm<sup>2</sup> area standard silicon photonics platform. To this author's knowledge, the prototype switch discussed herein has the largest port-count among the silicon photonic switches ever reported.

Movable directional couplers integrated on the optical crossbar network facilitated a high extinction ratio (25 dB) and fast switching speed (2.5  $\mu$ s response time), as well as the large scalability of the switch. An experimental demonstration showed that integration of MEMS technology into silicon photonics platform has the potential to benefit greatly integrated optics technology.

## ACKNOWLEDGMENTS

This work was supported in part by the National Science Foundation Center for Integrated Access Network (CIAN) under grant #EEC-0812072, National Science Foundation Center for Energy Efficient Electronics Science (E3S) under NSF Award 0939514, and Defense Advanced Research Project Agency (DARPA)'s Electronic-Photonic Heterogeneous Integration (E-PHI) program.

## REFERENCES

- [1] G. Porter, R. Strong, N. Farrington, A. Forencich, P. Chen-Sun, T. Rosing, Y. Fainman, G. Papen, and A. Vahdat, "Integrating Microsecond Circuit Switching into the Data Center," *ACM SIGCOMM Comput. Commun. Rev.*, vol. 43, no. 4, pp. 447–458, 2013.
- [2] N. Farrington, G. Porter, S. Radhakrishnan, H. H. Bazzaz, V. Subramanya, Y. Fainman, G. Papen, and A. Vahdat, "Helios : A Hybrid Electrical / Optical Switch Architecture for Modular Data Centers," *ACM SIGCOMM Comput. Commun. Rev.*, vol. 40, no. 4, pp. 339–350, 2010.
- [3] B. G. Lee, A. V Rylyakov, W. M. J. Green, S. Assefa, C. W. Baks, R. Rimolodonadio, D. M. Kuchta, M. H. Khater, T. Barwicz, C. Reinholm, E. Kiewra, S. M. Shank, C. L. Schow, and Y. A. Vlasov, "Monolithic Silicon Integration of Scaled Photonic Switch Fabrics, CMOS Logic, and Device Driver Circuits," *J. Light. Technol.*, vol. 32, no. 4, pp. 743–751, 2014.
- [4] S. K. Selvaraja, W. Bogaerts, and D. Van Thourhout, "Loss reduction in silicon nanophotonic waveguide micro-bends through etch profile improvement," *Opt. Commun.*, vol. 284, pp. 2141–2144, Apr. 2011.
- [5] M. M. Lee and M. C. Wu, "Thermal Annealing in Hydrogen for 3-D Profile Transformation on Silicon-on-Insulator and Sidewall Roughness Reduction," *J. Microelectromechanical Syst.*, vol. 15, no. 2, pp. 338–343, Apr. 2006.
- [6] R. T. Chen, H. Nguyen, and M. C. Wu, "A High-Speed Low-Voltage Stress-Induced Micromachined 2 x 2 Optical Switch," vol. 11, no. 11, pp. 1396–1398, 1999.
- [7] W. Young, R. Budynas, and A. Sadegh, *Roark's formulas for stress and strain*, 8th ed. McGraw-Hill, 2011.
- [8] G. J. O. Brien, D. J. Monk, and L. Lin, "MEMS cantilever beam electrostatic pull-in model," *SPIE*, vol. 4593, pp. 31–41, 2001.